Supporting Information for

Strategic Molecular Conformation Engineering Enables Significantly Enhanced High-Temperature Energy Storage in Polyetherimide

Xianhui Dong [a], Yan Wang [a], Jiabin Fu [a], Hao Zhang [b], Na Li [a, *], Yan Wang [a], Junrong Yu [a], Zuming Hu [a, *]

[1] *State Key Laboratory of Advanced Fiber Materials, College of Materials Science and Engineering, Donghua University, Shanghai 201620, China*

[2] *Sinochem International Corporation, Shanghai 200126, China*

[*] Corresponding author

E-mail addresses: linadhu@dhu.edu.cn (N. Li); hzm@dhu.edu.cn (Z. Hu).

1. Characterization

The ^{1}H and ^{19}F NMR spectra of the monomer and polymer precursor were obtained using a nuclear magnetic resonance spectrometer (NMR, 400 MHz, Bruker), with DMSO-d_6 as the solvent. The identification of functional groups in the monomer and all polymer films was performed using a Fourier-transform infrared spectrometer (FTIR, TensorFlow II). The surface and cross-sectional morphologies of all polymer films were observed using scanning electron microscopy (SEM, Zeiss Gemini 560). The XRD patterns were recorded using an X-ray diffractometer (XRD, D8 Advance, λ = 1.5418 Å) at 40 kV and 40 mA. The glass transition temperature (T_g) of all films was measured by differential scanning calorimetry (DSC, 204F1) under nitrogen atmosphere at a heating rate of 10 °C /min. The thermal stability was evaluated by thermogravimetric analysis (TGA, 209F1) under nitrogen atmosphere at a heating rate of 20 °C/min. The storage modulus of all polymer films was measured by dynamic mechanical analyzer (DMA 1, Mettler Toledo) in air from room temperature to 200 °C, with a heating rate of 5 °C/min and a frequency of 1 Hz. The ultraviolet-visible (UV-Vis) absorption spectra were acquired using an ultraviolet-visible near-infrared spectrophotometer (UV-3600, Shimadzu) over the 200-800 nm range. The surface roughness and modulus distribution of the polymer films were determined by atomic force microscopy (AFM, Bruker) operating in nanomechanical mapping mode.

Copper electrodes 20 mm in diameter were deposited on both film surfaces by thermal evaporation for subsequent dielectric measurements. The dielectric constant and dielectric loss of all dielectric films were systematically measured with a broadband dielectric impedance spectrometer (Novocontrol Concept 40) over the temperature range of 20 to 200 °C and the frequency range of 10^2 to 10^6 Hz. The breakdown strength of all films was measured using a DC withstand voltage instrument (CS9916BX, Nanjing Changsheng Instrument Co., Ltd.). All samples were fully immersed in silicone oil during testing. The voltage was raised at a ramp rate of 500 V/s until the film broke down completely. Each sample was tested at least 15 times and the experimental results were analyzed using two-parameter Weibull statistics. Gold

electrodes 3 mm and 5 mm in diameter were sputtered onto both sides of the polymer film for leakage current density, thermally stimulated depolarization current (TSDC), and capacitive energy storage performance measurements. The leakage current density at elevated temperature was recorded by the Radiant Technologies Premier II test system with a voltage amplifier Trek 610E. The electric displacement-electric field (*D-E*) loops were recorded using a ferroelectric analyzer (PK-FERRO20B, PolyK Technologies) at 10 Hz. During the TSDC measurement, the samples were initially polarized at 230 °C for 30 min with an electric field of 50 MV/m, and then rapidly cooled to -50 °C using liquid nitrogen under the sustained polarization electric field. Finally, the samples were short-circuited and heated to 250 °C at a rate of 3 °C/min, and the temperature-depolarization current relationship was recorded using the Novocontrol Concept 40 system.

2. Molecular dynamics (MD) simulation

Based on the chemical structures of the different polymers, the repeat units of PEI and PEI-FFDA were first built using Materials Studio software. After that, PEI and PEI-FFDA models were constructed with the AC module, and all models were subjected to geometry optimization in the Forcite module to obtain locally stable conformations. To eliminate configurational biases, an annealing and gradual relaxation strategy was employed to ensure the entire system reached a state of thermodynamic equilibrium. Briefly, under constant temperature and constant pressure (NPT), each polymer model was first subjected to five annealing cycles between 298 K and 598 K, followed by 500 ps of molecular dynamics simulation to release internal stress and drive the model to its lowest energy state.[1] Calculations were performed using the COMPASS II force field combined with the Smart optimization algorithm, with temperature regulated by a Nose thermostat. Electrostatic interactions were handled by the Ewald method, while van der Waals interactions were described using an atom-based approach with a 12.5 Å cutoff.[2] Finally, the fractional free volume was calculated from the stable polymer configuration (Fig. S10) using the following

equation:

$$FFV = \frac{V_F}{V_F + V_C} \times 100\% \quad \text{(S1)}$$

Where V_F and V_C represent the free volume and the occupied volume of the polymer cell, respectively.

3. Density functional theory (DFT) calculation

First, the molecular structures of PEI and PEI-FFDA were constructed and visualized using GaussView 6.0 software. Subsequently, the Gaussian 16W program was used to optimize their ground-state geometries using density functional theory (DFT) at the B3LYP/6-31G(d) level, and frequency analysis confirmed the structures to be global minima. Based on the optimized molecular structures, three-dimensional electrostatic potential distribution of the molecular models was calculated, and the highest occupied molecular orbital (HOMO) and the lowest unoccupied molecular orbital (LUMO) were analyzed.

The Multiwfn 3.8 program was further employed to perform statistical analysis of the electrostatic potential distribution and to generate the interfragment electron transition density matrix (TDM).[3] In characterizing the electronic excitation properties, the first five excited states were selected to describe electron transfer processes among the polymer units (hydrogen atoms were excluded from the calculations). The TDM describing electron transfer between different fragments can be expressed as:

$$\mathrm{p} \equiv \begin{matrix} \text{electron} \\ \\ \text{hole} \end{matrix} \begin{bmatrix} 1,N & 2,N & \cdots & N,N \\ \vdots & \vdots & \ddots & \vdots \\ 1,2 & 2,2 & \cdots & N,2 \\ 1,1 & 2,1 & \cdots & N,1 \end{bmatrix} \quad \text{(S2)}$$

In the above matrix, a dominant diagonal element (N, N) signifies that electron and hole are co-localized on fragment N, indicating the localized excitation.

Conversely, pronounced off-diagonal elements (M, N) imply that the hole resides primarily on fragment M while the electron is localized on fragment N, indicating a distinct charge transfer excitation from M to N.

Subsequently, the Multiwfn 3.8 program was employed to map the electron-hole distribution, localized orbital localization function (LOL), and the electron localization function (ELF) of PEI and PEI-FFDA.[4,5] For electron-hole distribution analysis, the exciton spatial extent over the molecular model was quantitatively characterized using the S_r, D, H, $\Delta\sigma$ and t parameters.

Specifically, S_r describes the average spatial overlap between the electron and hole distributions, and this index can be calculated as follows:

$$S_r(r) = \int \sqrt{\rho^{hole}(r)\rho^{ele}(r)}dr \quad \text{(S3)}$$

Where ρ^{hole} and ρ^{ele} represent the distributions of the hole and the electron, respectively, and r is the coordinate vector. A smaller S_r value indicates more significant spatial separation between the electron and hole, thereby characterizing a stronger charge-transfer (CT) character within the system.

D is an index that reflects the distance between the centroids of the hole and electron, and it can be expressed as:

$$D = \sqrt{(X_{ele} - X_{hole})^2 + (Y_{ele} - Y_{hole})^2 + (Z_{ele} - Z_{hole})^2} \quad \text{(S4)}$$

Where X_{ele}, Y_{ele}, Z_{ele} are the centroid coordinates of the electron, and X_{hole}, Y_{hole}, and Z_{hole} represent the centroid coordinates of the hole, respectively. A larger separation between the electron and hole centroids corresponds to a higher D value, signifying a weaker Coulombic interaction and thus facilitating charge transfer.

The $\Delta\sigma$ index quantifies the overall difference in spatial extent between the electron and the hole. The formula for Δσ is given by:

$$\Delta\sigma = |\sigma_{ele}| - |\sigma_{hole}| \quad \text{(S5)}$$

Where σ_{ele} and σ_{hole} denote the spatial spans of the electron and hole,

respectively. A larger $\Delta\sigma$ reflects a greater spatial separation between the electron and hole.

H index denotes the average spatial extent of the electron and hole distributions; it can be expressed as:

$$H = \left[\left(|\sigma_{ele}| + |\sigma_{hole}|\right)\right]/2 \quad \text{(S6)}$$

To account for spatial correlation effects along the charge transport direction, the t index is employed to adjust the centroid separation of electron-hole distributions, and the corresponding parametric equation can be written as:

$$t = D - H_{CT} \quad \text{(S7)}$$

Where H_{CT} represents the average spatial extent of the hole and electron along the charge-transfer direction. A smaller t indicates a more pronounced overlap between the electron and hole.

4. Simulation of temperature distribution in capacitor

The temperature distribution of film capacitors containing PEI and PEI-FFDA-5 films was simulated using the commercial COMSOL Multiphysics software. The stimulation process was conducted according to the following heat transfer model,

$$\rho C\frac{\partial T}{\partial t} = K\nabla^2 T + Q \quad \text{(S8)}$$

where ρ, C, K, and Q represent the density, specific heat capacity, thermal conductivity, and thermal power density, respectively. Specifically, Q was calculated by the energy loss with the equation $Q =$ $U_{\text{loss}}f$, where U_{loss} is the energy loss at 100 MV/m and f is the test frequency. The capacitor was set as a cylindrical with a height of 20 mm and a diameter of 20 mm. The simulated ambient temperature was set to 473.15 K and the boundary condition was set to convective heat flux with a heat transfer coefficient of 120 W m^{-2} K^{-1}.[6]

5. Calculation for the trap parameter from TSDC curve

In detail, the trap energy level can be calculated from the TSDC curve as:

$$A_{TSDC} = \frac{2.47 K_B T_P^2}{\Delta T} \tag{S9}$$

Where T_p and ΔT represent the temperature at peak current and temperature difference at half-peak height. Meanwhile, the trapped charge quantity corresponding to the trap energy level can be further calculated as:

$$Q_{TSDC} = \left(\frac{60}{v}\right)\int_{T_0}^{T_1} I(T)dT \tag{S10}$$

Where v, T_0, T_1, and $I(T)$ denote the heating rate after short-circuiting the samples, starting temperature of current peak, ending temperature of current peak, and the TSDC curve, respectively.[7]

6. Hopping conduction model

In this model, the current density (J) can be expressed as:

$$J(E,T) = 2ne\lambda v \times \exp\left[-\left(\frac{W_a}{K_B T}\right)\right] \times \sinh\left(\frac{\lambda eE}{2K_B T}\right) \tag{S11}$$

where n, e, λ, v, W_a, K_B, and T represent the carrier density, electric charge, hopping distance, attempt-to-escape frequency, activation energy, Boltzmann constant, and absolute temperature, respectively. At a fixed temperature, this can be simplified to:

$$J(E) = A\sinh(BE) \tag{S12}$$

where A and B are two lumped parameters. The λ value can be calculated by fitting J-E curves. It's worth noting that a decrease in λ value represents a higher trap depth is formed within the dielectric film.[8]

7. Calculation for the energy storage performance parameters

7.1 Characteristic breakdown strength

The characteristic breakdown strength of polymer dielectrics can be evaluated using the parameters of the two-parameter Weibull distribution as follows:

$$P(E) = 1 - exp\left[- \left({}^{E}/_{E_b} \right)^{\beta} \right] \tag{S12}$$

Where $P(E)$ represents the cumulative probability of electric-breakdown failure, E is the experimentally measured breakdown strength, and E_b is the characteristic breakdown strength at the failure probability of 63.2%. Additionally, β is the shape factor that reflects the dispersion of E.[9]

7.2 Discharge energy density (U_d) and efficiency (η)

The charge energy density (U), discharge energy density (U_{dis}), and charge-discharge efficiency (η) of all PEI films were calculated according to the *D-E* loops as follows:

$$U = \int_{0}^{D_{max}} E dD \tag{S13}$$

$$U_{dis} = \int_{D_r}^{D_{max}} E dD \tag{S14}$$

$$\eta = U_{dis}/U \times 100\% \tag{S15}$$

where E, D, D_{max}, and D_r are the applied electric field, electric displacement, maximum, and remnant electric displacement, respectively.[10]

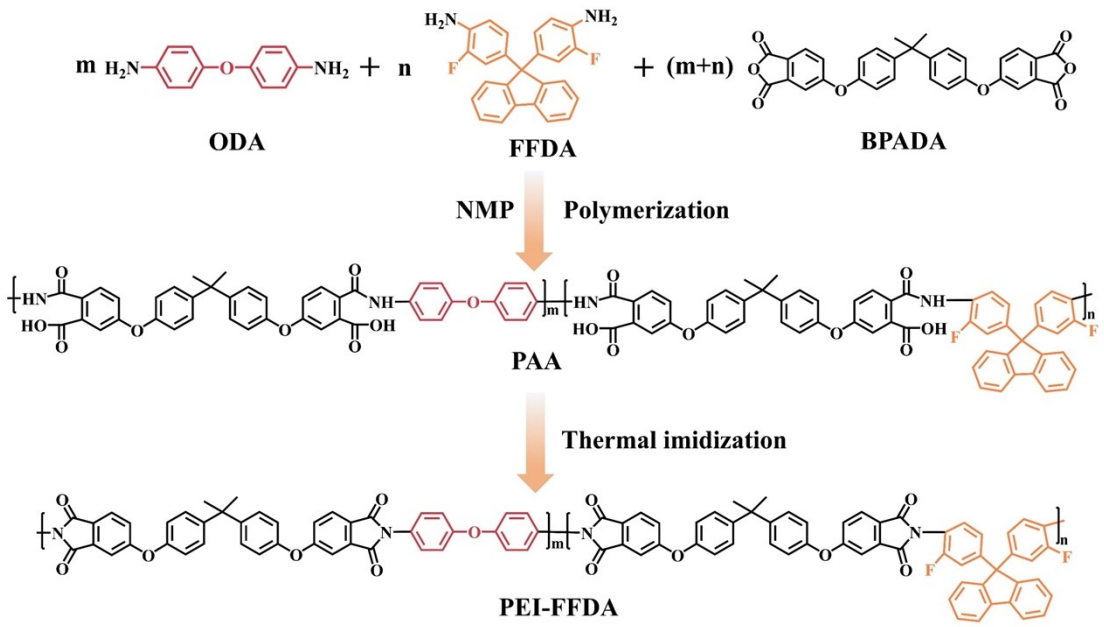

Fig. S1. Synthesis pathway of PEI-FFDA through thermal imidization.

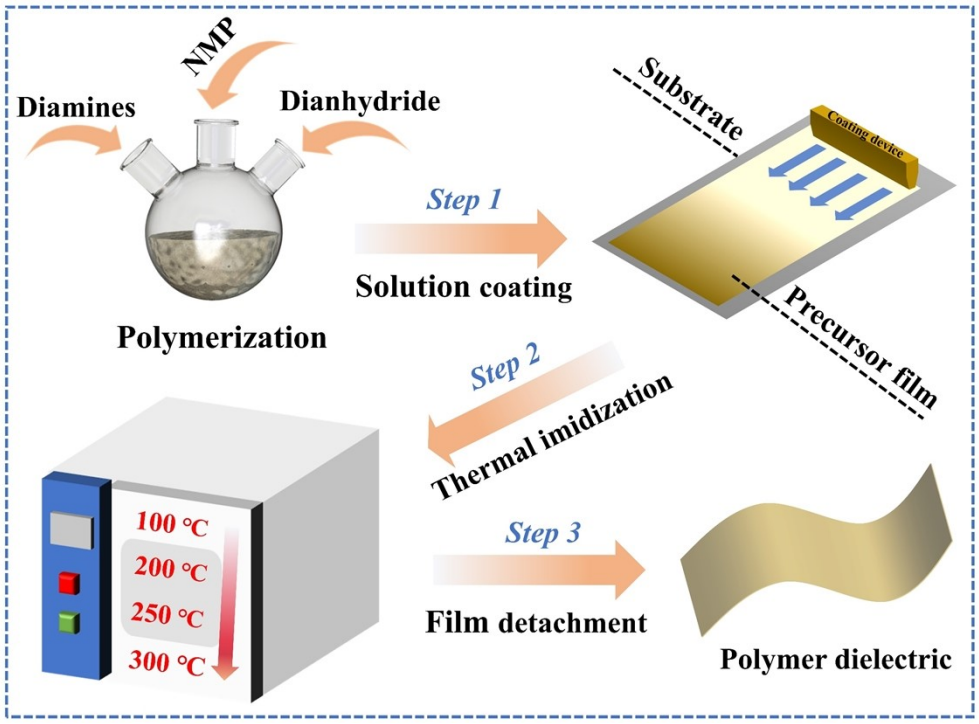

Fig. S2. Schematic diagram of the preparation process of polymer dielectric film.

Fig. S3. Optical photographs of the PEI-FFDA-5 film.

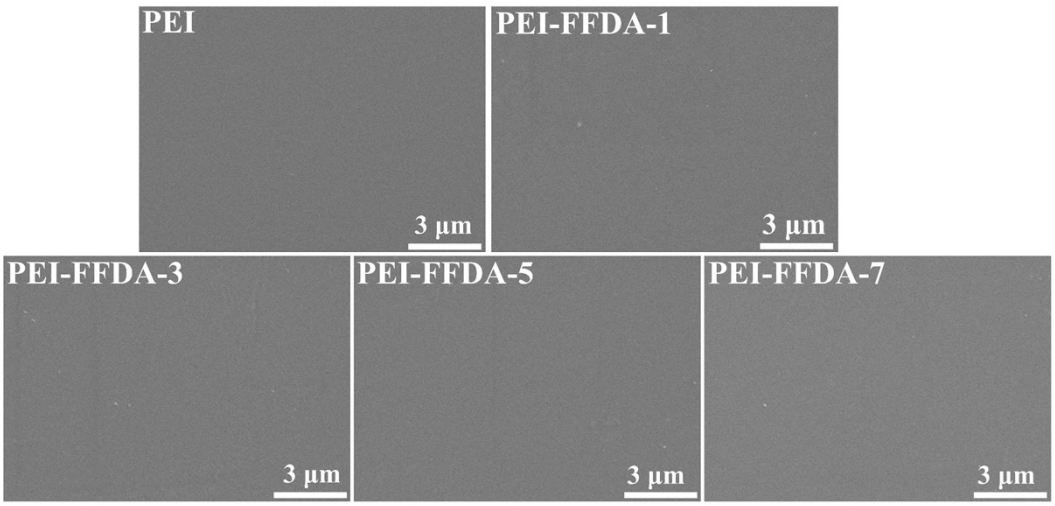

Fig. S4. Surface SEM images of PEI and PEI-FFDA films.

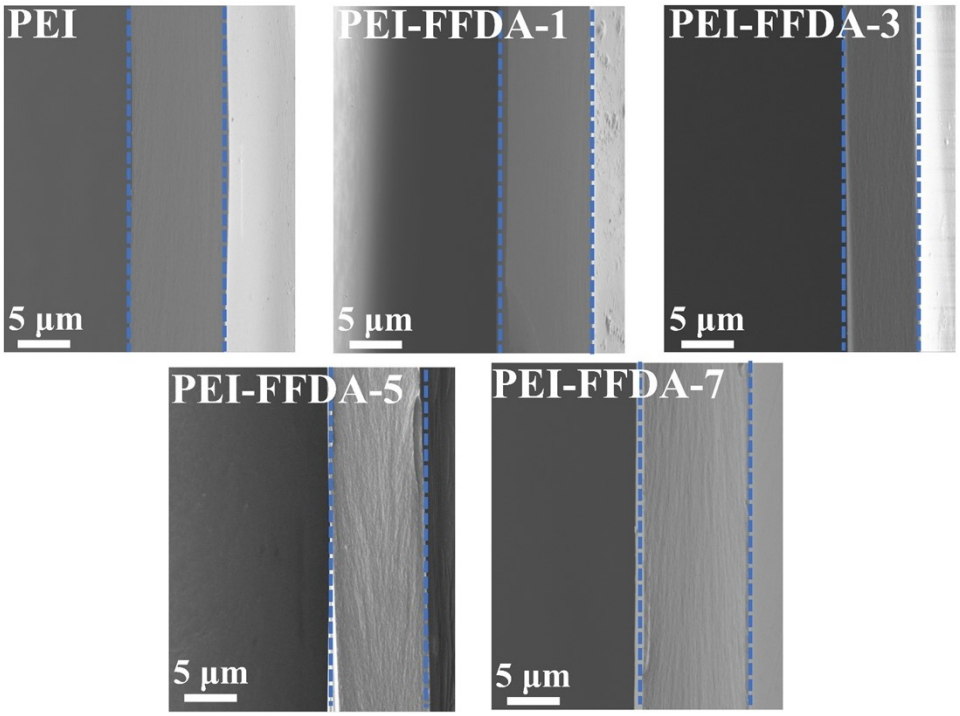

Fig. S5. Cross-sectional SEM images of PEI and PEI-FFDA films.

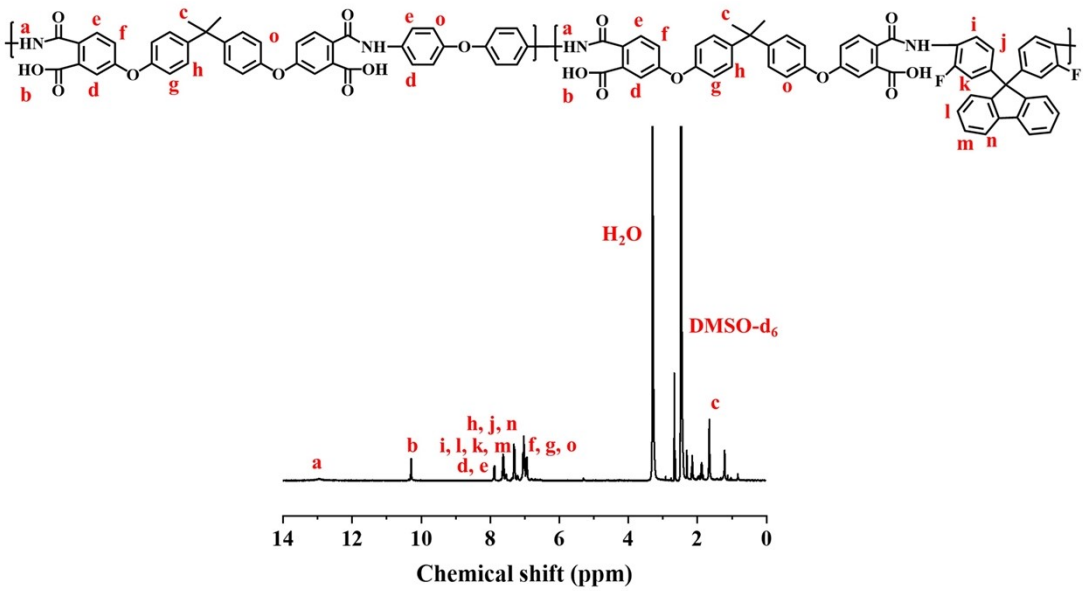

Fig. S6. ^{1}H NMR spectrum of poly(amic acid) (PAA) corresponding to PEI-FFDA.

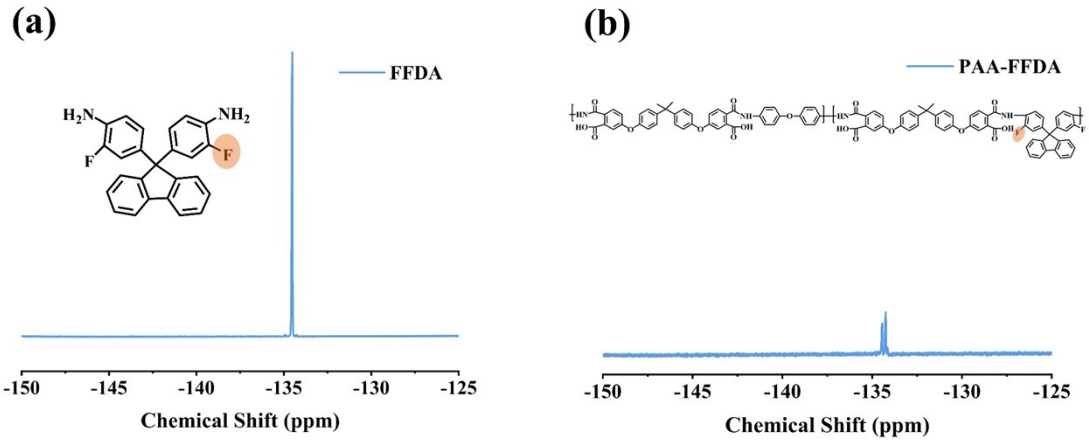

Fig. S7. ^{19}F NMR spectrum of (a) FFDA monomer and (b) PAA (corresponding to PEI-FFDA).

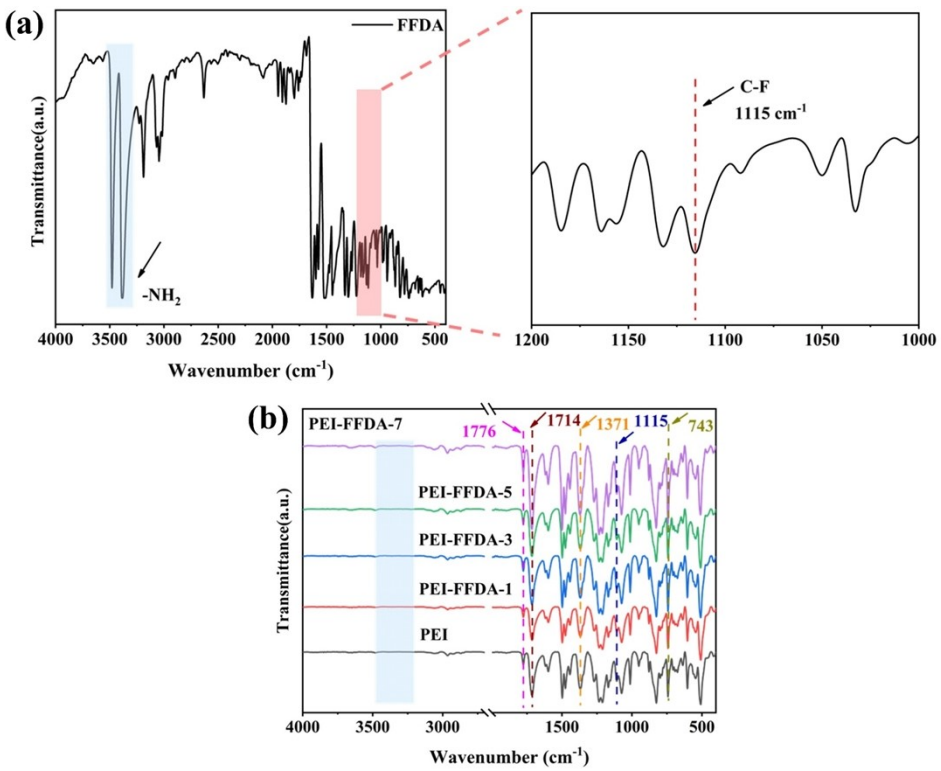

Fig. S8. FTIR spectra of (a) FFDA monomer and (b) all PEI films.

In the FTIR spectrum of FFDA diamine (Fig. S8a), the characteristic absorption peaks of -NH_2 groups were observed in the range of 3200-3500 cm^{-1}, while the peak at 1115 cm^{-1} is attributed to the C-F stretching vibration.[11] Following copolymerization and subsequent thermal imidization, it can be found from the FTIR spectra (Fig. S8b) in polymer films that the appearance of characteristic peaks at 743 cm^{-1}, 1371 cm^{-1}, 1714 cm^{-1} and 1776 cm^{-1}, which correspond to the bending vibration of C=O, stretching vibration of C-N, symmetric and asymmetric stretching of C=O in imide groups, respectively.[12] Moreover, the disappearance of -NH_2 stretching vibration peak and emergence of C-F bond characteristic peak demonstrate that the FFDA until has been successfully integrated into the PEI molecular chains.

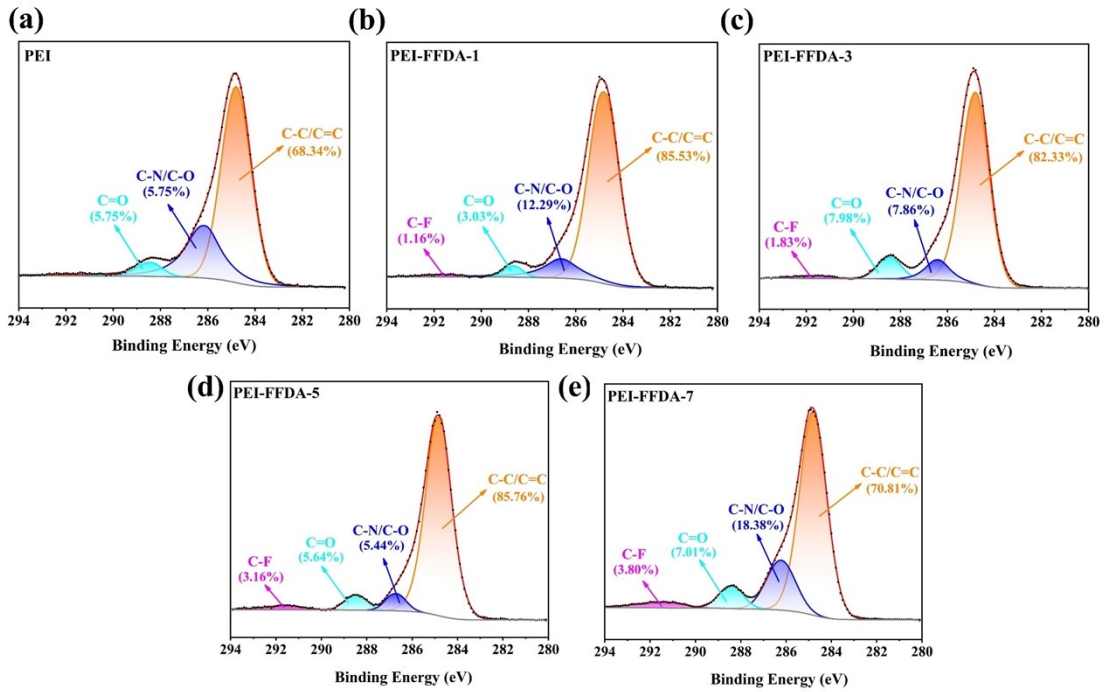

Fig. S9. High-resolution XPS spectrum of the C 1s region for (a) PEI, (b) PEI-FFDA-1, (c) PEI-FFDA-3, (d) PEI-FFDA-5, and (e) PEI-FFDA-7.

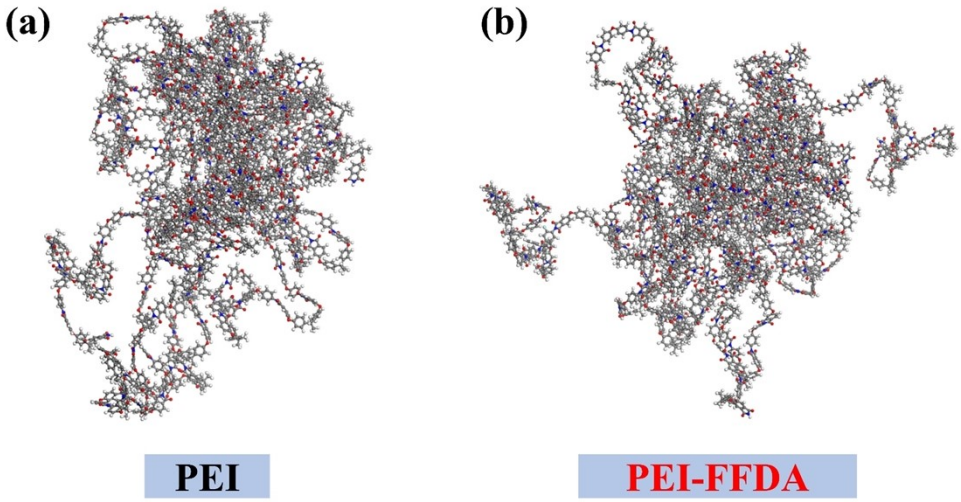

Fig. S10. Obtained polymer models of (a) PEI and (b) PEI-FFDA-5 after the molecular dynamic simulation.

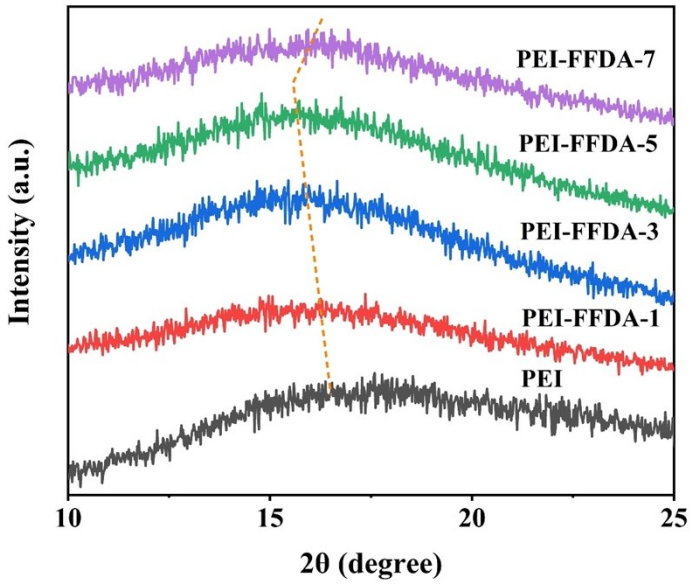

Fig. S11. XRD patterns of PEI and PEI-FFDA dielectric films.

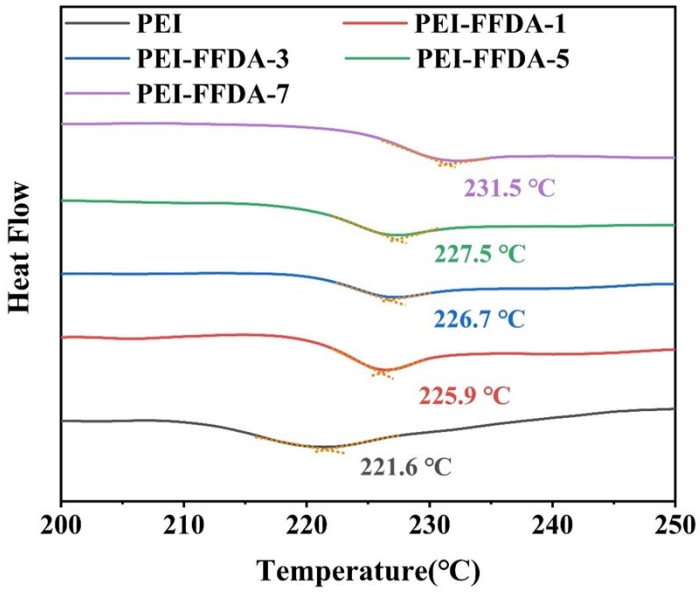

Fig. S12. DSC curves of PEI and PEI-FFDA films.

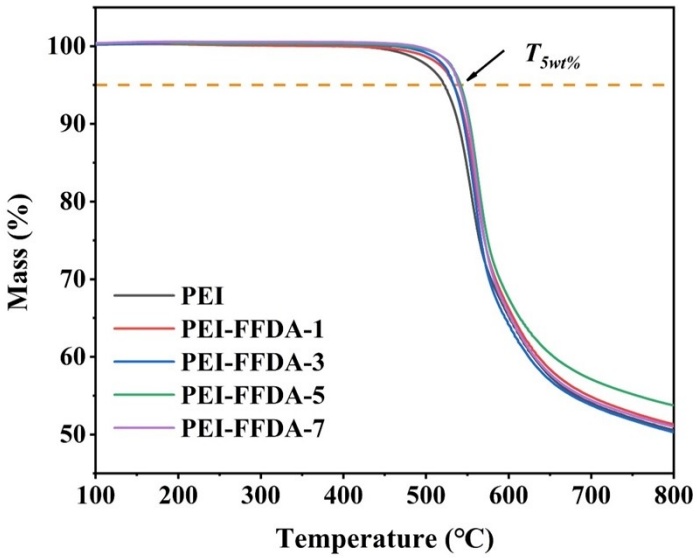

Fig. S13. TG curves of PEI and PEI-FFDA films.

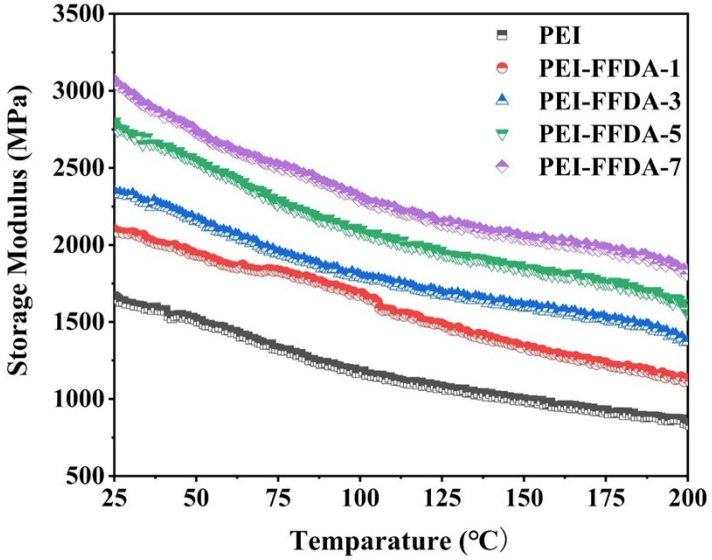

Fig. S14. Temperature dependence of storage modulus of PEI and PEI-FFDA films.

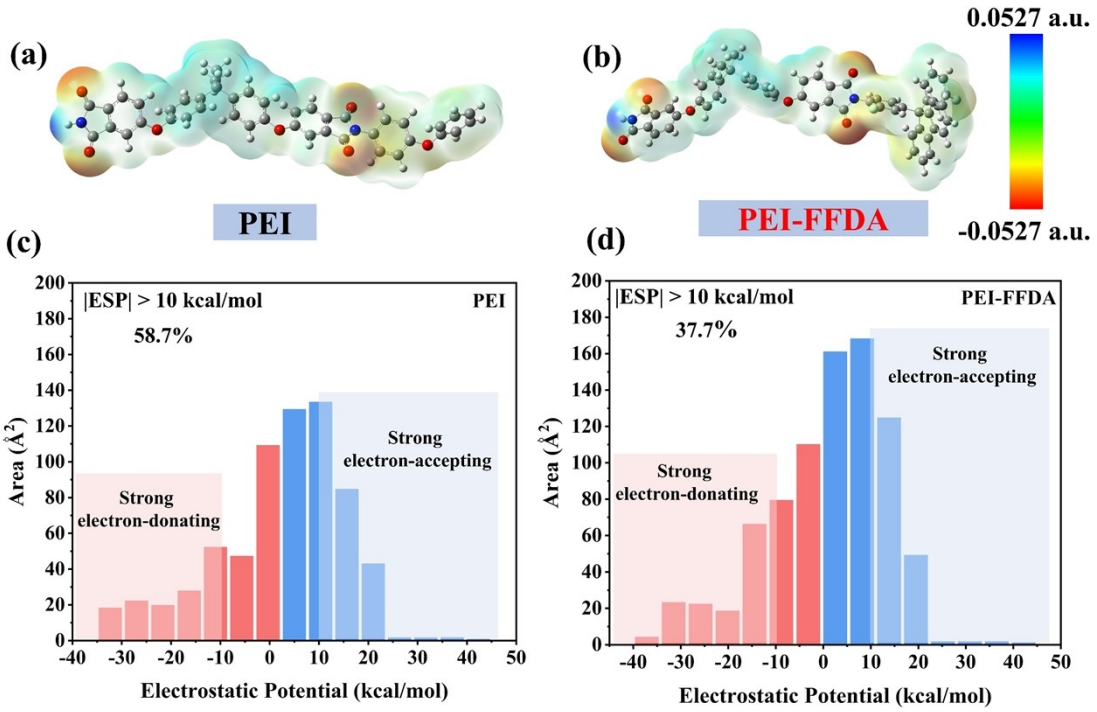

Fig. S15. Electrostatic potential distribution in molecular chain of (a) PEI and (b) PEI-FFDA. Statistical electrostatic potential area distribution characteristics of (c) PEI and (d) PEI-FFDA

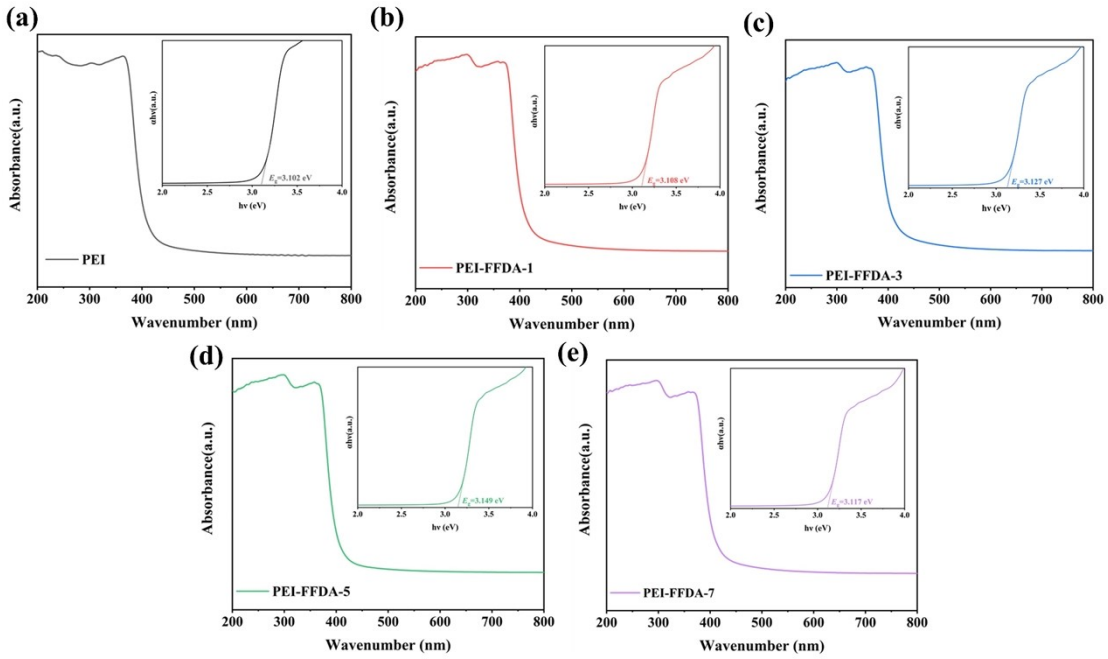

Fig. S16. UV-Vis spectra of (a) PEI, (b) PEI-FFDA-1, (c) PEI-FFDA-3, (d) PEI-FFDA-5, and (e) PEI-FFDA-7. The relationship between $(\alpha h\nu)^2$ and $h\nu$ was analyzed by the Tauc plot to calculate the optical bandgap.[13]

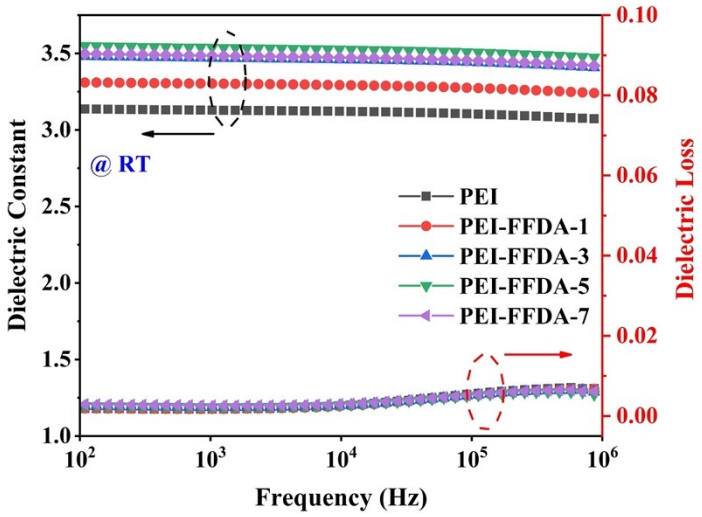

Fig. S17. Frequency dependence of dielectric constant and dielectric loss of PEI and PEI-FFDA at room temperature.

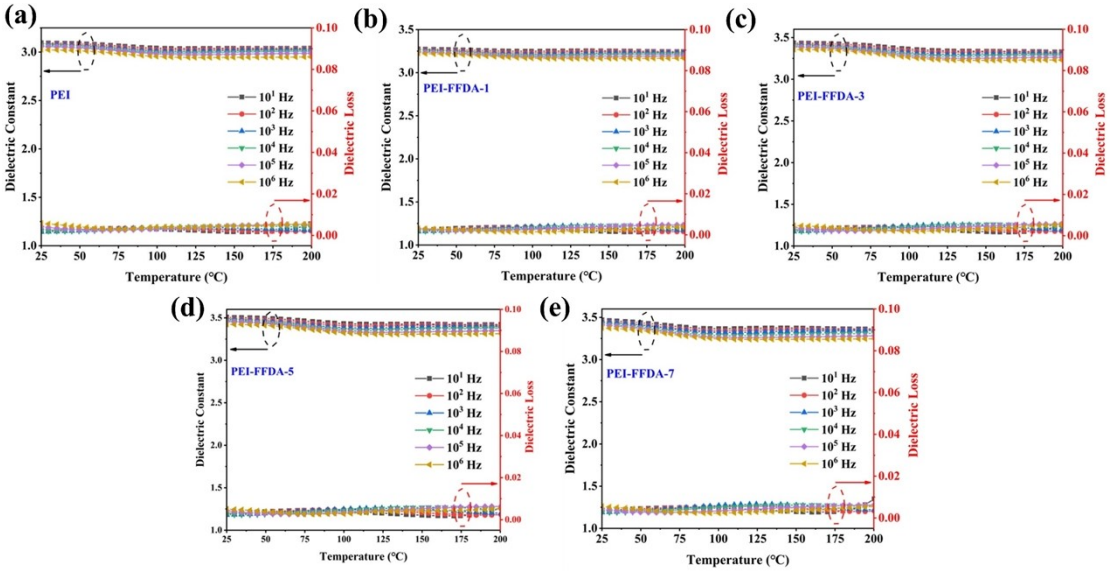

Fig. S18. Temperature dependence of dielectric constant and dielectric loss of (a) PEI, (b) PEI-FFDA-1, (c) PEI-FFDA-3, (d) PEI-FFDA-5, and (e) PEI-FFDA-7 at different frequencies.

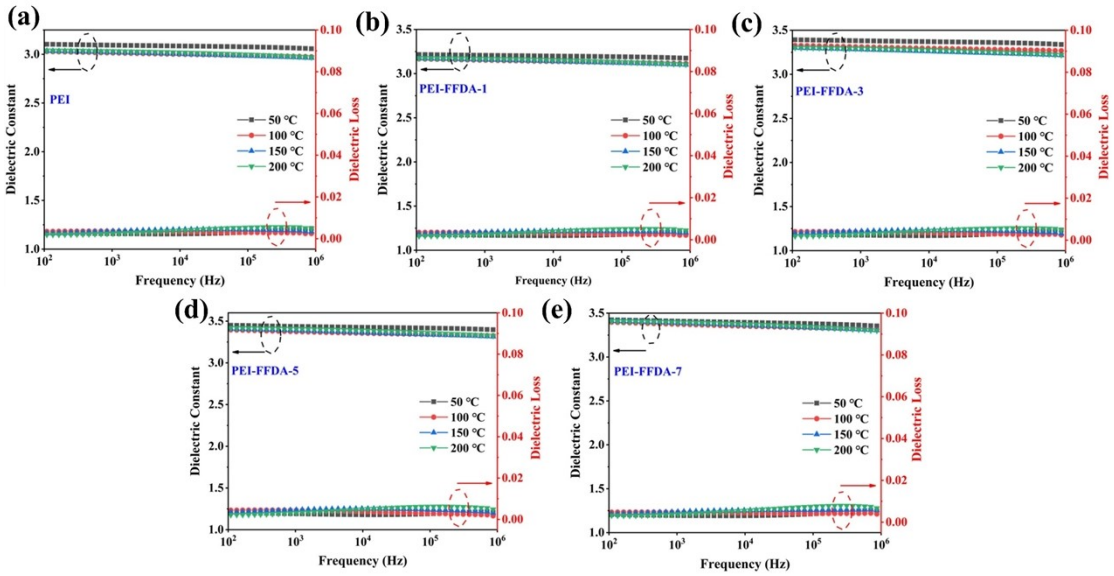

Fig. S19. Frequency dependence of dielectric constant and dielectric loss of (a) PEI, (b) PEI-FFDA-1, (c) PEI-FFDA-3, (d) PEI-FFDA-5, and (e) PEI-FFDA-7 at different temperatures.

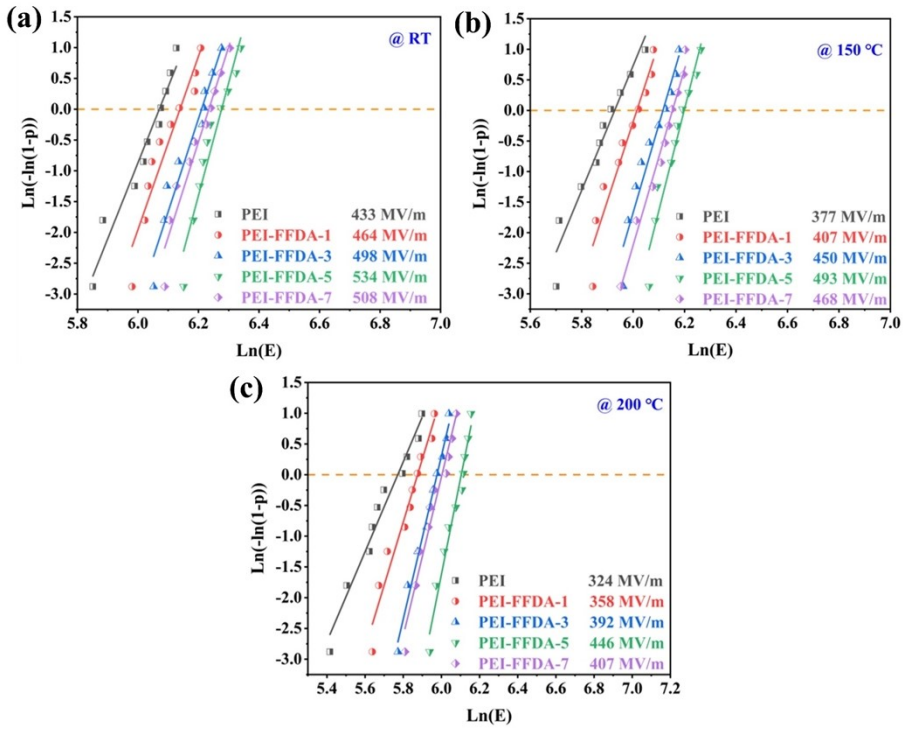

Fig. S20. Weibull breakdown strengths of PEI and PEI-FFDA at (a) room temperature, (b) 150 °C, and (c) 200 °C, respectively.

Table S1. Statistical E_b and β values for PEI and PEI-FFDA at different temperatures. The molar ratio was defined as the mole percentage of FFDA diamine in the total diamine content of the polymerization system.

	Molar Ratio	**0**	**1%**	**3%**	**5%**	**7%**
RT	E_b **(MV/m)**	433	464	498	534	508
	β	12.3	14.1	15.1	18.3	15.4
150 °C	E_b **(MV/m)**	377	407	450	493	468
	β	10.2	12.9	14.4	16.7	14.4
200 °C	E_b **(MV/m)**	324	358	392	446	407
	β	7.3	10.3	13.3	15.6	12.9

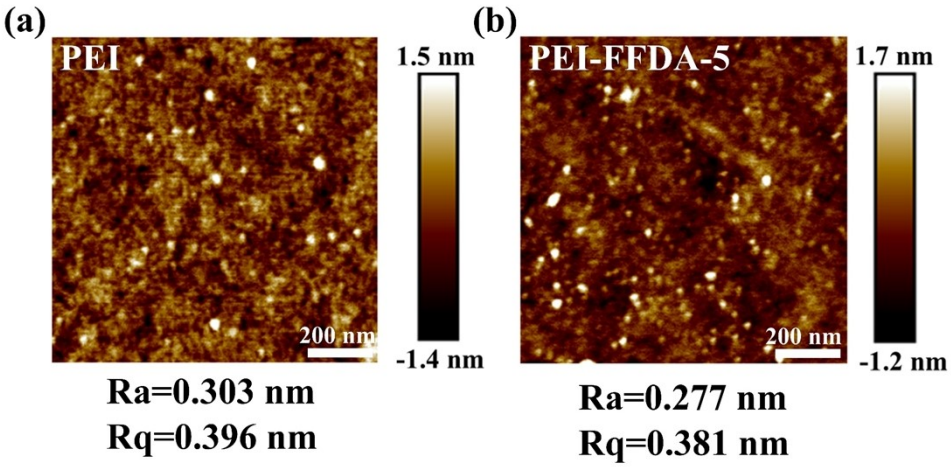

Fig. S21. AFM surface morphology images of (a) PEI and (b) PEI-FFDA-5 films. Ra and Rq represent the arithmetic average roughness and root mean square roughness, respectively.

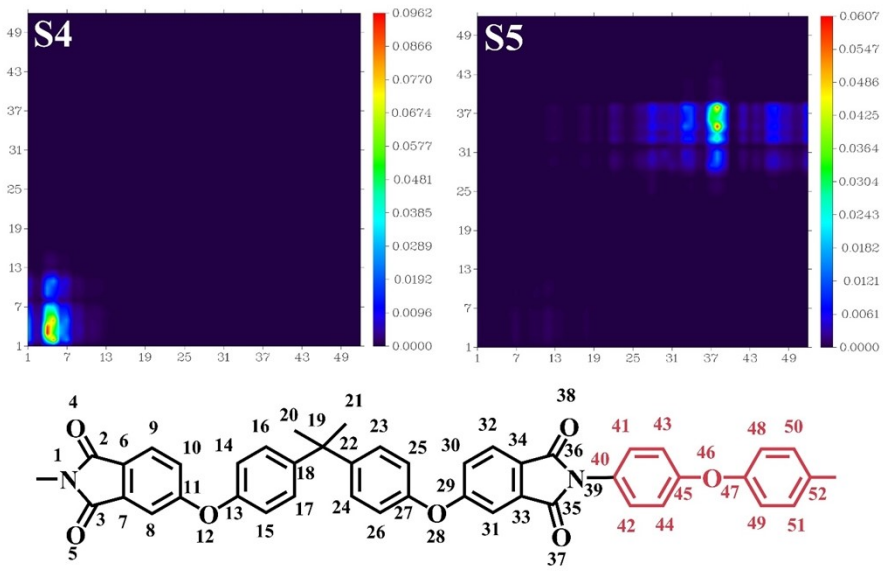

Fig. S22. TDM calculations for PEI in S4 and S5 excited states.

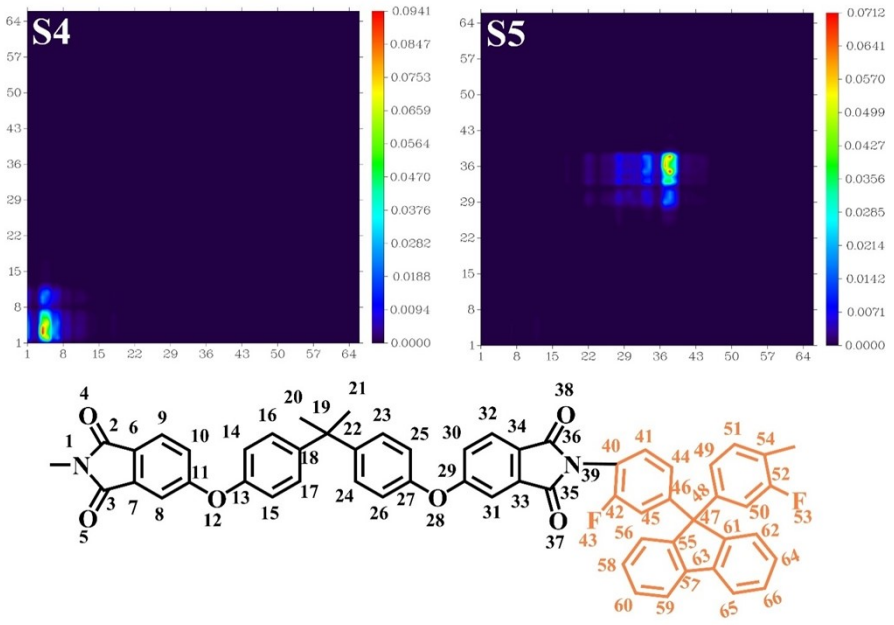

Fig. S23. TDM calculations for PEI-FFDA in S4 and S5 excited states.

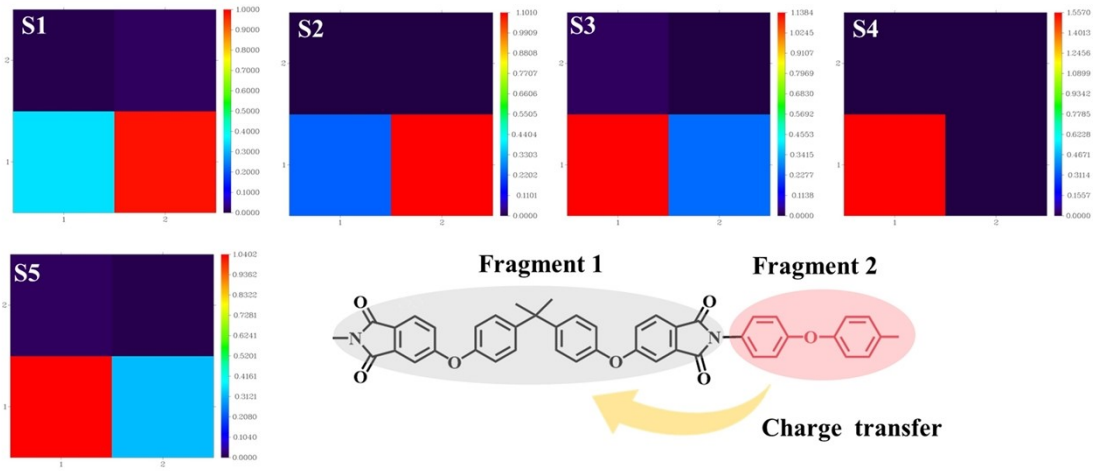

Fig. S24. TDM calculations between dianhydride and diamine in PEI at different excited states. To describe the electron transfer characteristics between fragments, we defined the dianhydride moiety in the PEI as Fragment 1 and the diamine moiety as Fragment 2.

Table S2. Intra- and interfragment electron transfer amounts in different excited states for PEI.

	PEI			
States	**1→1 (e)**	**1→2 (e)**	**2→1 (e)**	**2→2 (e)**
S1	0.345	0.007	0.981	0.016
S2	0.235	0	1.101	0
S3	1.138	0.015	0.256	0.004
S4	1.557	2.2E-4	2.3E-4	4E-6
S5	1.040	0.016	0.320	0.005

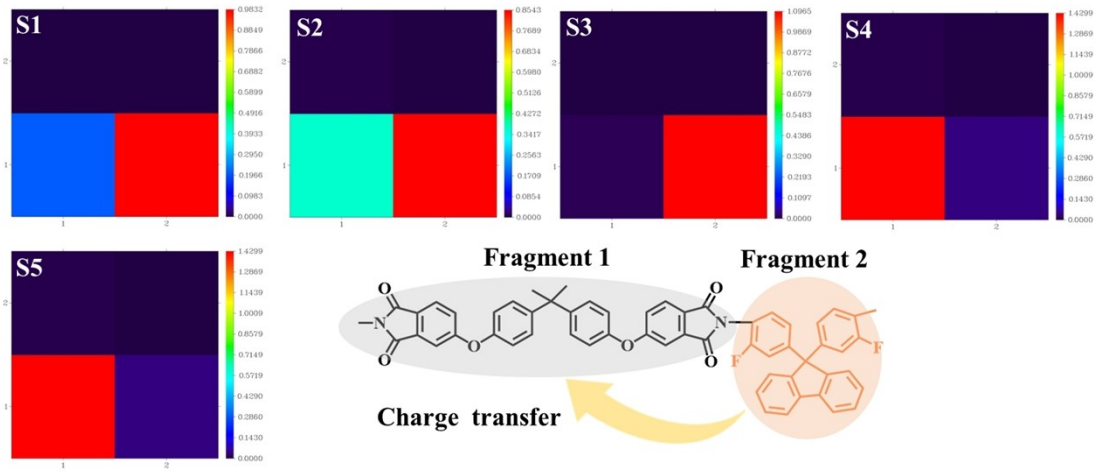

Fig. S25. TDM calculations between dianhydride and diamine in PEI-FFDA at different excited states. In the PEI-FFDA, the dianhydride moiety was defined as Fragment 1 and the diamine moiety as Fragment 2.

Table S3. Intra- and interfragment electron transfer amounts in different excited states for PEI-FFDA.

PEI-FFDA				
States	**1→1 (e)**	**1→2 (e)**	**2→1 (e)**	**2→2 (e)**
S1	0.206	0.002	0.983	0.003
S2	0.363	0.004	0.854	0.003
S3	0.012	0	1.097	0
S4	1.546	6.0E-4	2.5E-4	1.4E-5
S5	1.430	0.008	0.045	8.1E-4

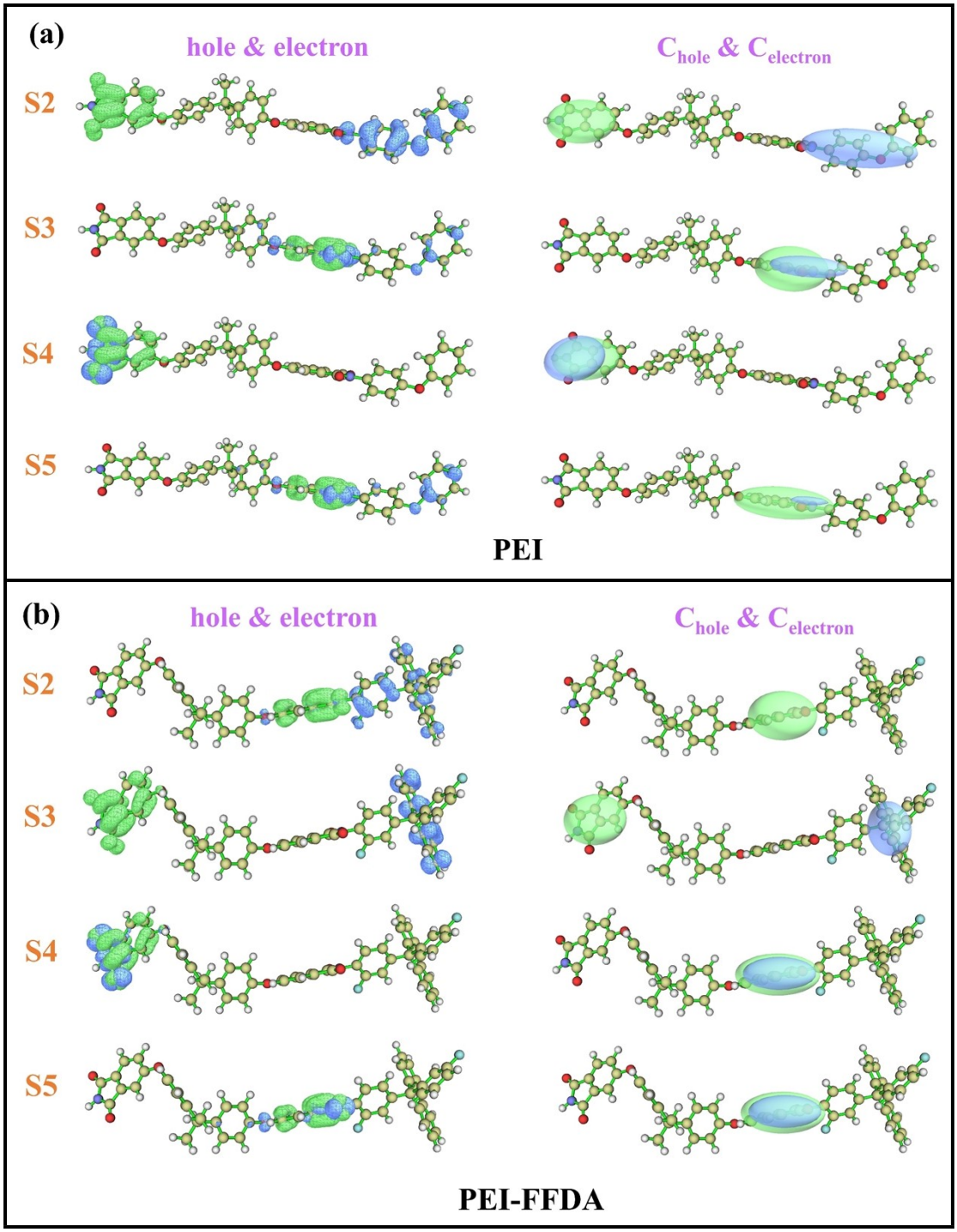

Fig. S26. Electronic-hole structures and C_{hole} & $C_{electron}$ plots of (a) PEI and (b) PEI-FFDA in different excited states.

Table S4. Excitation characteristic parameters of PEI in S1-S5 excited states.

PEI					
States	S_r **(a.u.)**	D **(Å)**	$\Delta\sigma$ **(Å)**	H **(Å)**	t **(Å)**
S1	0.332	4.57	-1.10	2.93	2.13
S2	0.010	22.88	-1.00	2.87	20.51
S3	0.545	1.38	-2.40	3.69	-1.74
S4	0.535	0.91	-0.18	2.49	-0.18
S5	0.514	2.09	-1.96	4.86	-2.34

Table S5. Excitation characteristic parameters of PEI-FFDA in S1-S5 excited states.

PEI-FFDA					
States	S_r **(a.u.)**	D **(Å)**	$\Delta\sigma$ **(Å)**	H **(Å)**	t **(Å)**
S1	0.257	6.52	-1.73	3.26	4.07
S2	0.347	5.08	-2.28	3.55	2.28
S3	0.002	23.90	-0.48	2.62	22.45
S4	0.543	0.82	-0.30	2.55	-0.63
S5	0.592	0.17	-0.64	3.39	-2.33

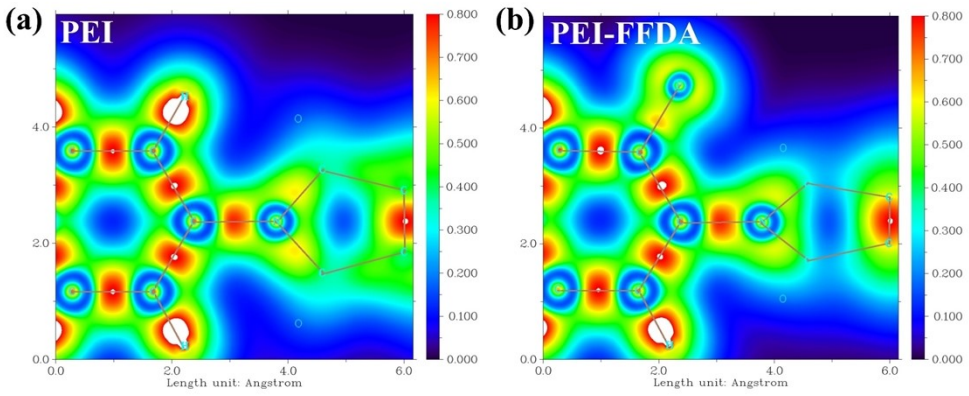

Fig. S27. Visualizations of LOL-π maps of (a) PEI and (b) PEI-FFDA.

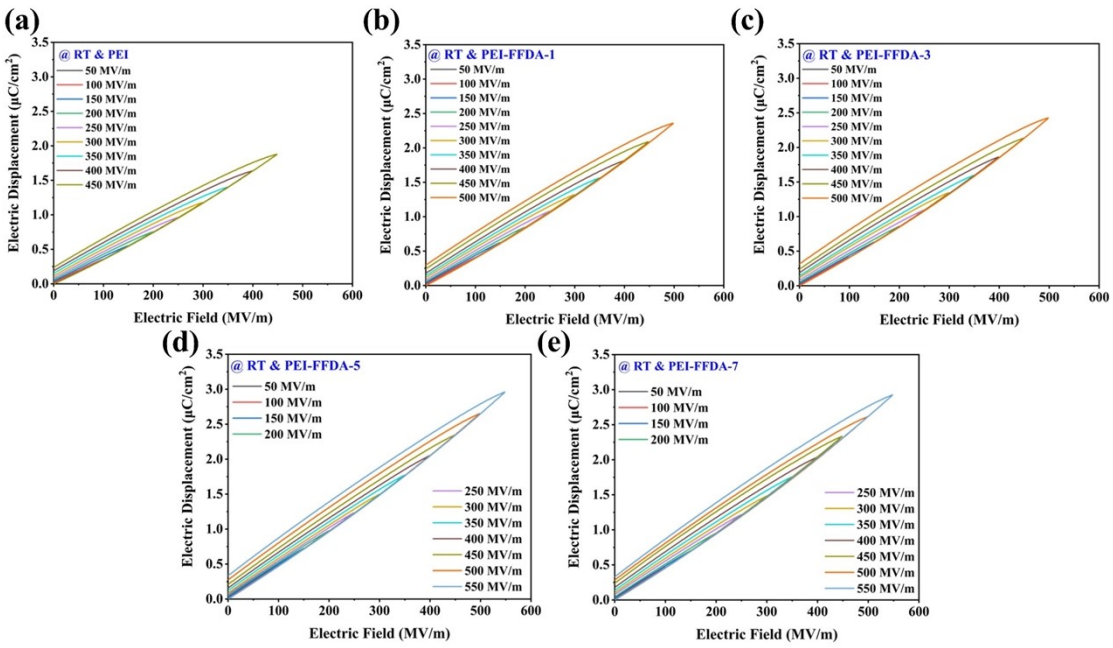

Fig. S28. *D-E* loops of (a) PEI, (b) PEI-FFDA-1, (c) PEI-FFDA-3, (d) PEI-FFDA-5, and (e) PEI-FFDA-7 at room temperature.

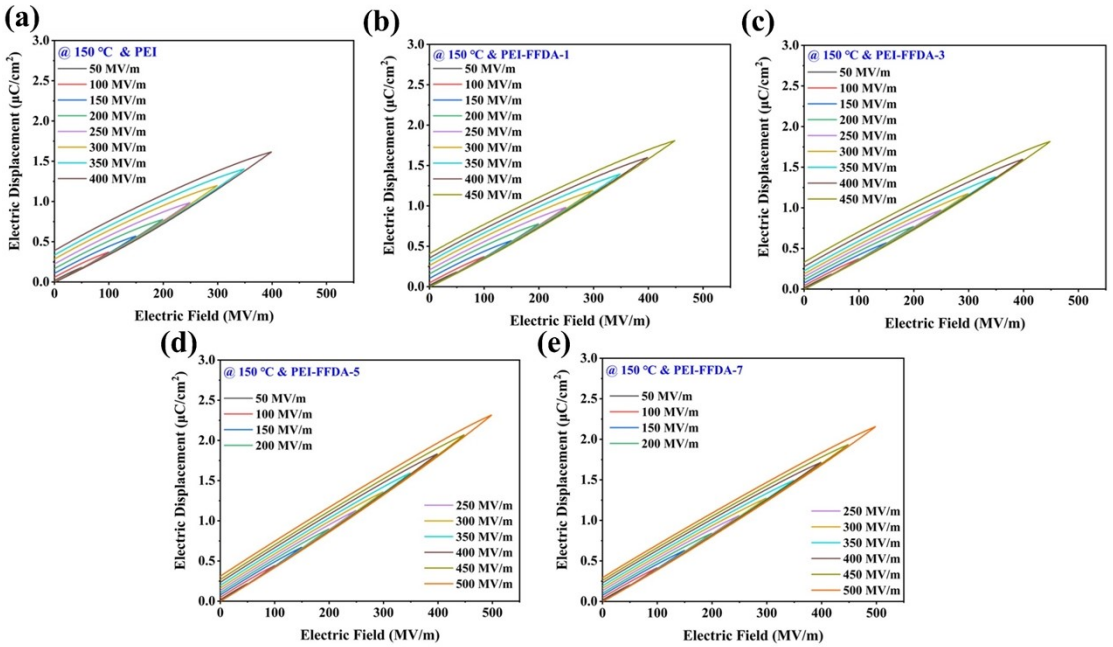

Fig. S29. *D-E* loops of (a) PEI, (b) PEI-FFDA-1, (c) PEI-FFDA-3, (d) PEI-FFDA-5, and (e) PEI-FFDA-7 at150 °C.

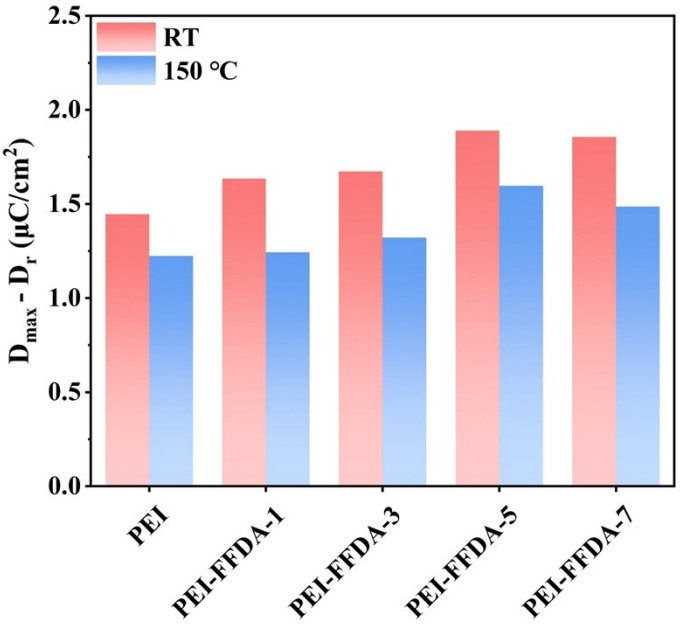

Fig. S30. Difference between maximum electric displacement and remnant electric displacement of PEI and PEI-FFDA films at room temperature and 150 °C. These results were obtained at 400 MV/m.

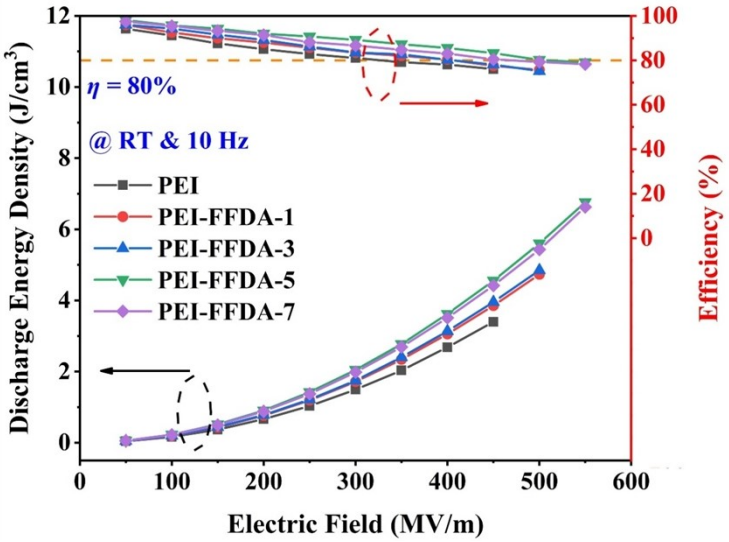

Fig. S31. Discharged energy density and charge-discharge efficiency of PEI and PEI-FFDA versus electric field at room temperature.

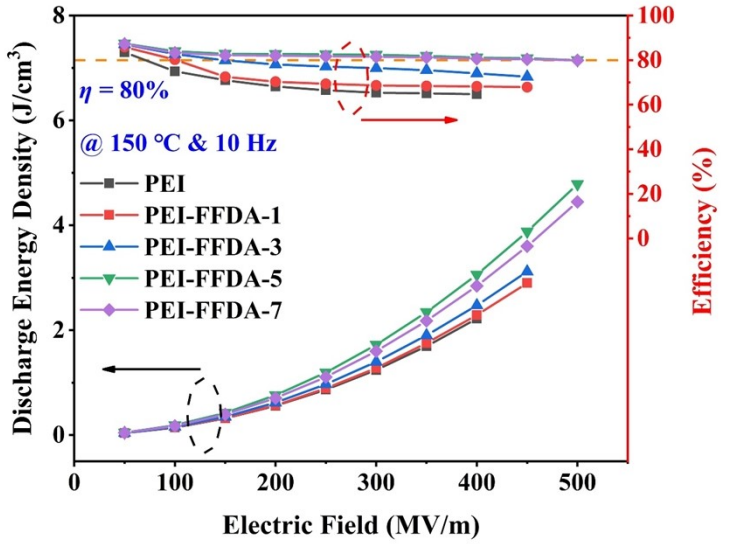

Fig. S32. Discharged energy density and charge-discharge efficiency of PEI and PEI-FFDA versus electric field at 150 °C.

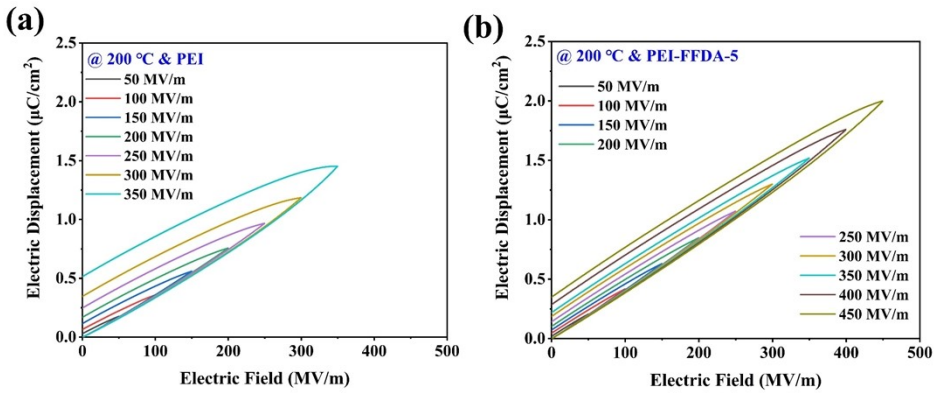

Fig. S33. *D-E* loops of (a) PEI and (b) PEI-FFDA-5 at 200 °C.

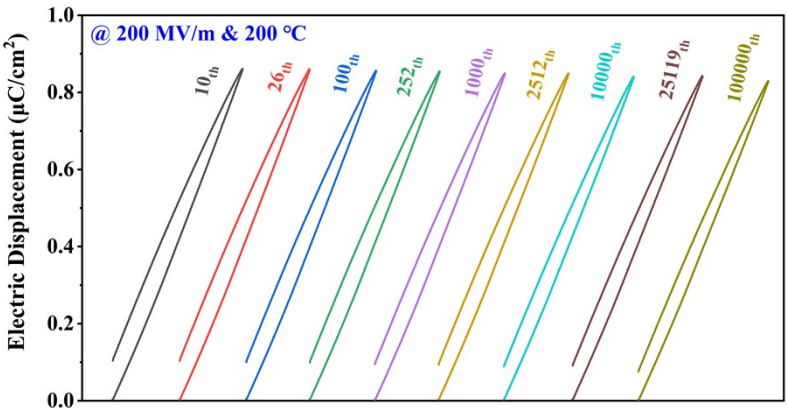

Fig. S34. *D-E* loops of PEI-FFDA-5 in different cycle numbers at 200 °C and 200 MV/m.

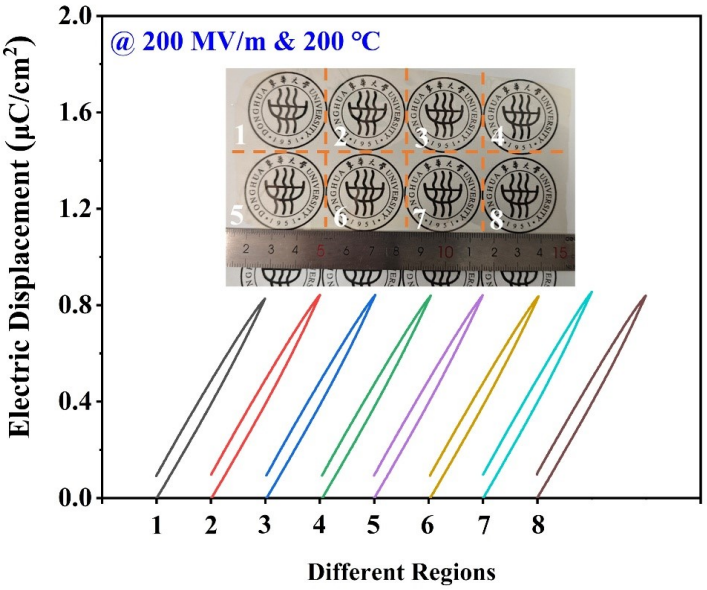

Fig. S35. Optical photo of PEI-FFDA-5 large-size film, and *D-E* loops at different test regions at 200 °C and 200 MV/m.

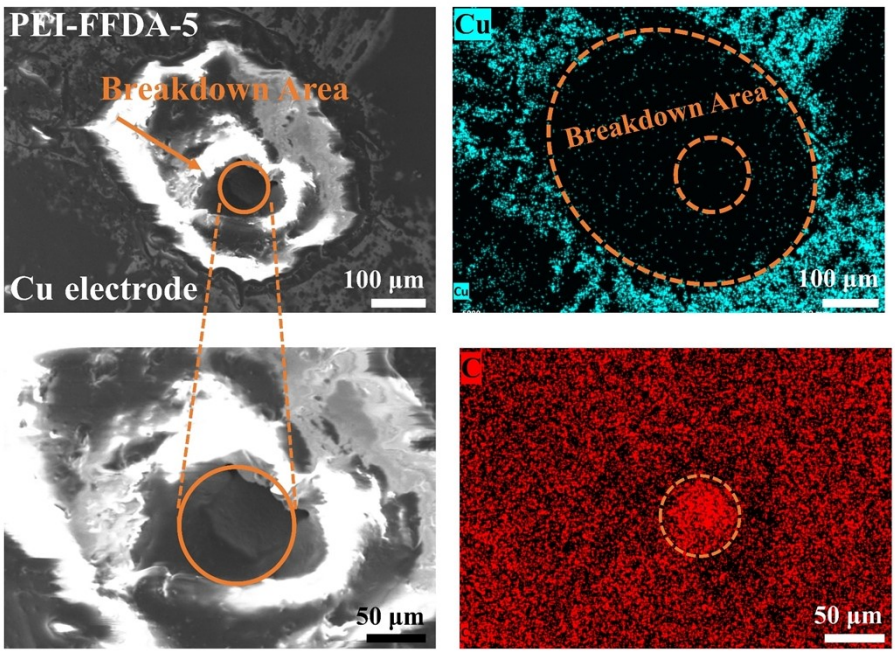

Fig. S36. SEM images of the metallized PEI-FFDA-5 film after dielectric breakdown, along with the corresponding EDS elemental mappings of Cu and C.

As revealed by SEM observation in Fig. S36, the sample exhibits a distinct penetrating breakdown hole accompanied by a broad electrode evaporation zone after dielectric breakdown. This morphological evolution is primarily driven by the instantaneous vaporization of the polymer matrix triggered by intense Joule heating, coupled with the thermal ablation of the metal electrode induced by the local high temperature of the electric arc. Energy dispersive X-ray spectroscopy (EDS) mapping indicates that the Cu map shows a clear absence of signals around the breakdown point, proving the intense evaporation and recession of the electrode, which is essential for self-healing.[14] Additionally, the C map reveals a strong signal at the center, attributed to the exposed underlying carbon conductive tape. Notably, the electrode recession area is significantly larger than the breakdown hole itself, confirming that the conductive path is effectively interrupted by physical separation.

References

1 Y. Wan, H. Luo, Z. Yan, J. Peng, G. He, X. Li, F. Wang, Z. Ran, D. Zhang and Q. Li, *Adv. Mater.*, 2025, **37**, e10122.

2 F. Yin, L. Yang, Y. Mo, W. Hou and Y. Yuan, *Mater. Chem. Phys.*, 2022, **286**, 126008.

3 T. Lu and F. Chen, *J. Comput. Chem.*, 2012, **33**, 580–592.

4 X. Wang, Z. Liu, X. Yan, T. Lu, H. Wang, W. Xiong and M. Zhao, *Phys. Chem. Chem. Phys.*, 2022, **24**, 7466–7473.

5 Z. Liu, T. Lu and Q. Chen, *Carbon*, 2020, **165**, 461–467.

6 Z. Wang, Y. Zhao, M. Yang, H. Yan, C. Xu, B. Tian, C. Zhang, Q. Xie and Z. Dang, *Adv. Energy Mater.*, 2025, **15**, 2405411.

7 T. Zeng, D. Liu, G. Liu, L. Meng, F. Wang, Y. Li and C. Yuan, *Chem. Eng. J.*, 2026, **529**, 173165.

8 G. Duan, F. Hu, Y. He, Z. Hu, M. Tian and J. Zha, *J. Mater. Chem. A*, 2026, **14**, 548–559.

9 Y. Han, X. Li, Y. Liu, J. Qian, J. Liu, D. Xu, W. Zhao, H. Zhou, J. Zhai, T. Zhou, Y. Zhou, W. Liu and D. Zhou, *Nano Energy*, 2026, **147**, 111587.

10 J. Chen, X. Li, Z. Yan, H. Luo and D. Zhang, *J. Energy Storage*, 2025, **140**, 118965.

11 W. Sima, Y. Mai, P. Sun, M. Yang, T. Yuan, B. Chen and Y. Yang, *Energy Storage Mater.*, 2025, **74**, 103974.

12 D. Ai, C. Wu, Y. Han, Y. Chang, Z. Xie, H. Yu, Y. Ma, Y. Cheng and G. Wu, *J. Mater. Sci. Technol.*, 2025, **210**, 170–178.

13 M. Liu, J. Song, H. Qin, S. Qin, Y. Zhang, W. Xia, C. Xiong and F. Liu, *Adv. Funct. Mater.*, 2024, **34**, 2313258.

14 W. Huang, B. Wan, X. Yang, M. Cheng, Y. Zhang, Y. Li, C. Wu, Z. Dang and J. Zha, *Adv. Mater.*, 2024, **36**, 2410927.